Acta Crystallographica Section A
Foundations of Crystallography
ISSN 0108-7673

Received 6 June 2012
Accepted 8 November 2012

© 2013 International Union of Crystallography
Printed in Singapore – all rights reserved

Calculation of absorption and secondary scattering of X-rays by spherical amorphous materials in an asymmetric transmission geometry

J. C. Bendert,* M. E. Blodgett and K. F. Kelton

Department of Physics, Washington University, St Louis, Missouri 63130-4899, USA. Correspondence e-mail: jbendert@physics.wustl.edu

Expressions for absorption and the secondary scattering intensity ratio are presented for a small beam impinging off-center of a spherical amorphous sample. Large gradients in the absorption correction are observed from small offsets from the central axis. Additionally, the secondary scattering intensity ratio causes an intensity asymmetry in the detector image. The secondary scattering intensity ratio is presented in integral form and must be computed numerically. An analytic, small-angle, asymptotic series solution for the integral form of the absorption correction is also presented.

1. Introduction

Levitation techniques, including electrostatic levitation, electromagnetic levitation and conical nozzle levitation, have been developed for the study of liquids in an inert, contactless environment. The absence of a container removes a major source of heterogeneous nucleation and allows studies of liquids in the supercooled state (*i.e.* below the equilibrium melting temperature). Recently, these levitation techniques have been used for laboratory X-ray, synchrotron and neutron scattering studies of these supercooled liquids (Masaki *et al.*, 2007; Egry & Holland-Moritz, 2011; Gangopadhyay *et al.*, 2005; Mauro & Kelton, 2011; Krishnan *et al.*, 1997; Higuchi *et al.*, 2007; Aoki *et al.*, 2003). Owing to surface-tension effects, the liquids are nearly spherical in shape. A transmission geometry is typically used for the scattering studies. In many cases, the beam size is smaller than the sample size, so that previously reported spherical corrections cannot be applied for the analysis of the data. Beam alignment becomes critical in these cases; off-axis transmission through the spherical samples can result in asymmetric scattering. Although precision alignment stages for levitation chambers have been reported (Mauro & Kelton, 2011), variations in sample size and density can cause positional variation between measurements. Some method for correcting for the resulting asymmetric scattering is needed to compare measurements.

Secondary scattering and absorption corrections for standard geometries [*i.e.* plane sample reflection (Warren & Mozzi, 1966; Dwiggins & Park, 1971), transmission (Dwiggins & Park, 1971) and moving sample transmission (Dwiggins, 1972) as well as cylindrical sample transmission (Paalman & Pings, 1962; Blech & Averbach, 1965)] are well known. Although absorption corrections for small- (Zeidler, 2012) and large- (Dwiggins, 1975) diameter X-ray beams incident on spherical samples have been reported, neither secondary scattering corrections nor absorption corrections for off-axis transmission through spherical samples have ever been previously reported. These corrections are presented in this paper, giving the integral forms of absorption and secondary scattering intensity through a given solid angle by an amorphous spherical sample from an off-axis, infinitesimal, partially polarized X-ray beam. An analytic approximation is also reported for the absorption correction in the small-angle limit for rapid computation.

2. Theory

The theory of X-ray absorption and secondary scattering correction for arbitrary sample shapes, for the transmission geometry shown in Fig. 1, is derived in this section. For notation used in this paper, see Table 1.

As shown in Fig. 1(*a*), the infinitesimal scattered intensity $\mathrm{d}I(r, 2\theta, \phi)$ at some distance r from an infinitesimal scattering volume $\mathrm{d}V$ is given by

$$\mathrm{d}I(r, 2\theta, \phi) = I_0 \frac{\sigma_\mathrm{e} n}{r^2} P(\kappa_0, 2\theta, \phi) J(2\theta)\, \mathrm{d}V, \qquad (1)$$

where n is the average number density of the scattering element, I_0 is the intensity of the principal beam incident on the volume and $P(\kappa_0, 2\theta, \phi)$ accounts for polarization effects. The first-order scattering intensity $J(2\theta)$ is a combination of the coherent and incoherent scattering intensity in electron units. Since the coherent and incoherent electron cross sections are approximately equal, σ_e is the differential Thomson cross section for electrons, e^4/m^2c^4. Since only amorphous samples are considered, $J(2\theta)$ is assumed to be symmetric about the azimuthal angle ϕ. In this case, scattering asymmetry arises from polarization effects, $P(\kappa, 2\theta, \phi)$, which are described by

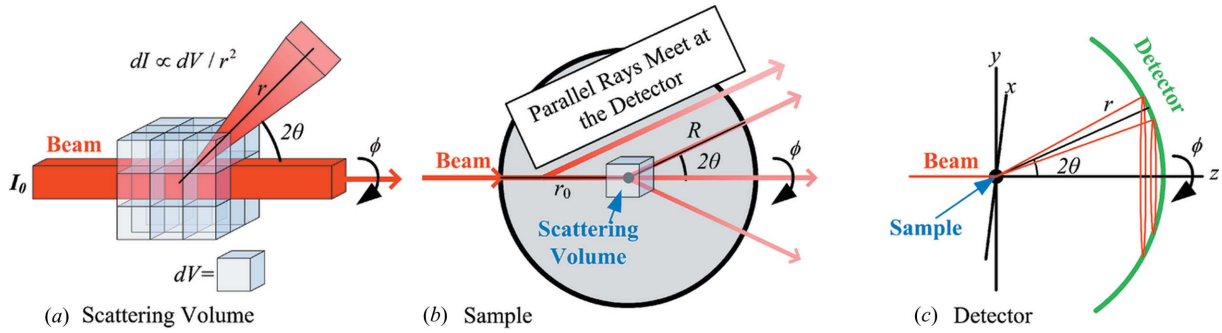

Figure 1
Transmission geometry viewed in different magnifications: (*a*) at differential volume length scales, (*b*) at sample length scales and (*c*) at detector length scales.

Table 1
Nomenclature.

I_0	Intensity of the principal beam incident on the sample
I_i	Intensity of a beam after the ith scattering event
σ_e	Differential electron scattering cross section
$P(\kappa, 2\theta, \phi)$	Angle-dependent attenuation due to polarization
κ	Polarization, defined as $(I_x - I_y)/(I_x + I_y)$
$J(2\theta)$	First-order scattering intensity in electron units
n	Number density
V	Ideal, unattenuated scattering volume
V'	Effective scattering volume due to attenuation
dV_1	Differential volume of the principal beam path, $dV_1 = dA_0 dr_0$
dV_2	Differential volume of the primary scattered beam path, $dV_2 = r_1^2 \cos(2\theta_1)\, d\phi_1\, d2\theta_1\, dr_1$
dA_0	Principal beam differential area $dA_0 = r' dr' d\phi'$
ϕ', r'	Principal beam azimuthal and radial coordinates
r_s and r_B	Sample and beam radii
ξ, ρ, z	Azimuthal and radial coordinates defining a distance from the central axis of a spherical sample, and the coordinate along the central axis
ξ_0, x	Azimuthal and radial coordinates defining beam center incidence on a spherical sample
R	Geometry- and angle-dependent path length from the final diffraction event to the edge of the sample
μ, μ'	Linear attenuation coefficient of the scattering material before and after energy shift due to a diffraction event
$\mathbf{R}$	Total scattering vector
r, ϕ, 2θ	Spherical coordinates of total scattering
$\mathbf{R}_i$	Vector path of the beam following the ith scattering event
r_i, ϕ_i, $2\theta_i$	Diffraction coordinates of the ith scattering event
O_i	A point defined by the path $\sum_j^i \mathbf{R}_{j-1}$
χ_i	Atom fraction of element i
Z_i	Atomic number of element i
M_i	Molar mass of element i
$(\mu/n)_i$	Mass absorption coefficient of element i
f_i	Atomic form factor of element i
$i(M)$	Incoherent scattering of element i
Subscript 's'	For any defined variable α, subscript 's' denotes a change in scale to units of sample radius such that $\alpha/r_s = \alpha_s$
N_A	Avogadro's number
N	Normalization constant to convert from measured intensity to electron units

$$P(\kappa, 2\theta, \phi) = 1/2 + \kappa[\sin(\phi)^2 - \cos(\phi)^2]/2 + \{1 + \kappa[\cos(\phi)^2 - \sin(\phi)^2]\}\cos(2\theta)^2/2, \quad (2)$$

where κ quantifies the polarization by the ratio of difference in intensity between the x and y components of the incident beam and the total intensity $(I_x - I_y)/(I_x + I_y)$ (Kahn *et al.*, 1982; Coppens *et al.*, 1992).

Far from the scattering event (Fig. 1*c*), the intensity measured at a solid angle, defined by 2θ and ϕ, is the integral of equation (1) over the scattering elements in the sample. The total number of scattering elements is the integral of equation (1) over the volume V for a homogeneous sample. For a non-absorbing material this intensity would be described by

$$I(r, 2\theta, \phi) = \frac{I_0 n}{r^2}\sigma_e P(\kappa_0, 2\theta, \phi) J(2\theta) V. \quad (3)$$

In reality, both the intensities of the incident beam and the scattered beam are attenuated as they travel through the material according to Beer's law, $I(r) = I(0)\exp(-\mu r)$, where $I(r)$ is the intensity a distance r into a material of attenuation coefficient μ. The first scattering intensity, accounting for this absorption, is given by equation (4), where, as shown in Fig. 1(*b*), r_0 is the path length of the incident beam to the differential scattering volume and R is the position- and solid-angle-dependent path length of the scattered beam,

$$I_1(r, 2\theta, \phi) = \left(I_0 n \sigma_e / r^2\right) \int_V \int \int dV \times \left\{P(\kappa_0, 2\theta, \phi) J(2\theta) \exp\left[-\mu r_0 - \mu' R(\Omega)\right]\right\}. \quad (4)$$

Equation (4) can be rewritten in the form of equation (3) by defining an effective scattering volume of the system as $V' = \int_V \int \exp[-\mu r_0 - \mu' R(\Omega)]\, dV$. Absorption corrections convert the measured effective scattering volume to that for the non-absorbing case by multiplying equation (4) by a factor of V/V'.

The scattered beam may, of course, continue to scatter within the sample. However, since each successive scattering event is less intense, only secondary scattering needs to be considered as a correction to recover the primary scattering intensity. A secondary scattering event is illustrated in Fig. 2, where an incident X-ray beam of intensity I_0 travels along the path $\mathbf{R}_0$.

As previously noted, absorption will cause the beam to be attenuated along $\mathbf{R}_0$, so that the intensity at the point O_1, where the beam is scattered, is given by

$$I_0(O_1) = I_0 \exp(-\mu r_0), \quad (5)$$

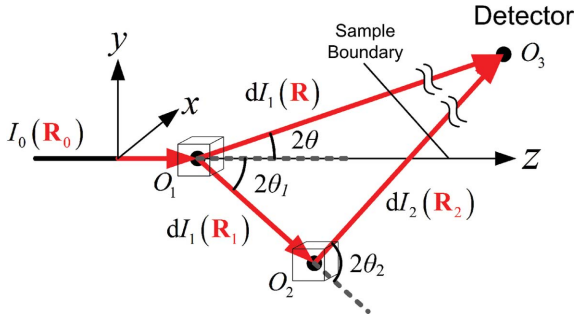

Figure 2
General diagram of secondary scattering.

where $|\mathbf{R}_0| = r_0$. The first scattered beam may either take a direct path $\mathbf{R}$ to the detector (point O_3) or reach the detector after having a secondary scattering event at O_2. The contribution of the primary scattering intensity from the differential volume at point O_1 is $dI_1(\mathbf{R})$ at point O_3. For a small sample far from the detector, the integral over parallel rays at angles 2θ and ϕ is the total primary scattering intensity at point O_3.

The intensity of the beam at O_2, scattered from O_1 and traveling a distance $\mathbf{R}_1$, is given by equation (6), where dV_1 is the differential scattering volume at point O_1 and κ_0 is the polarization state of the incident beam. If the scattering is inelastic, the absorption coefficient, μ', will differ from the original one. Since the change in energy is assumed to be small, for these calculations μ' can be set equal to μ.

$$dI_1(\mathbf{R}_0, O_2) = I_0(O_1)P(\kappa_0, 2\theta_1, \phi_1) \times \exp(-\mu' r_1)\frac{n}{{r_1}^2}\sigma_e J(2\theta_1)\,dV_1. \quad (6)$$

To be detected at point O_3, the beam must again scatter at O_2 so that it follows path $\mathbf{R}_2$. The differential intensity of the secondary scattered beam measured at O_3 is described by equation (7). The beam leaves the sample at some point along the path $\mathbf{R}_2$, but may also be attenuated by intermediate material (*i.e.* the exit window and air path); the changing attenuation coefficients along the path are represented as a path integral in the exponential argument,

$$dI_2(\mathbf{R}_0, \mathbf{R}_1, O_3) = \left(I_0 n^2 \sigma_e^2 / {r_1}^2 {r_2}^2\right) \exp\left[-\mu(r_0 + r_1) - \int_{O_2}^{O_3} \mu(x)\,dx\right] \times P(\kappa_0, 2\theta_1, \phi_1) J(2\theta_1) P(\kappa_1, 2\theta_2, \phi_2) J(2\theta_2)\,dV_1\,dV_2. \quad (7)$$

The first differential volume, dV_1, is the differential area of the principal beam, dA_0, multiplied by the differential path length dr_0, *i.e.* $dV_1 = dA_0 dr_0$. The second differential volume, dV_2, is described in terms of the diffraction coordinates of $\mathbf{R}_1$ by $dV_2 = {r_1}^2 \cos(2\theta_1)\,d\phi_1\,d2\theta_1\,dr_1$. From Fig. 2, the angles $2\theta_2$ and ϕ_2 describe the diffraction angles of the secondary scattering event.

For $|\mathbf{R}_2| \gg |\mathbf{R}_1|$ (far detector limit), $\mathbf{R} \simeq \mathbf{R}_2$, so that the secondary diffraction angles $2\theta_2$ and ϕ_2 map onto $\mathbf{R}$ by a $2\theta_1$ rotation about the y axis and then a ϕ_1 rotation about the z axis. The rotation matrix, equation (8), constrains $2\theta_2$ and ϕ_2, as shown in equations (9) and (10),

$$\begin{bmatrix} \sin(2\theta_2)\cos(\phi_2) \\ \sin(2\theta_2)\sin(\phi_2) \\ \cos(2\theta_2) \end{bmatrix} = \begin{bmatrix} \cos(2\theta_1)\cos(\phi_1) & \cos(2\theta_1)\sin(\phi_1) & -\sin(2\theta_1) \\ -\sin(\phi_1) & \cos(\phi_1) & 0 \\ \sin(2\theta_1)\cos(\phi_1) & \sin(2\theta_1)\sin(\phi_1) & \cos(2\theta_1) \end{bmatrix} \times \begin{bmatrix} \sin(2\theta)\cos(\phi) \\ \sin(2\theta)\sin(\phi) \\ \cos(2\theta) \end{bmatrix}. \quad (8)$$

$$\cos(2\theta_2) = \sin(2\theta_1)\cos(\phi_1)\sin(2\theta)\cos(\phi) + \sin(2\theta_1)\sin(\phi_1)\sin(2\theta)\sin(\phi) + \cos(2\theta_1)\cos(2\theta), \quad (9)$$

$$\tan(\phi_2) = \left[\cos(\phi_1)\sin(2\theta)\sin(\phi) - \sin(\phi_1)\sin(2\theta)\cos(\phi)\right] \times \left[\cos(2\theta_1)\cos(\phi_1)\sin(2\theta)\cos(\phi) + \cos(2\theta_1)\sin(\phi_1)\sin(2\theta)\sin(\phi) - \sin(2\theta_1)\cos(2\theta)\right]^{-1}. \quad (10)$$

The angle ϕ_2 only comes into the spherical geometry calculation through the secondary diffraction polarization term $P(\kappa_1, 2\theta_2, \phi_2)$. After the first scattering event, the polarization state of the beam changes, such that κ_1 is given by

$$\frac{\left[\kappa_0\cos^2(\phi_1) - \kappa_0\sin^2(\phi_1) + 1\right]\left[\cos^2(2\theta_1) + 1\right] - 2}{\left[\kappa_0\cos^2(\phi_1) - \kappa_0\sin^2(\phi_1) + 1\right]\left[\cos^2(2\theta_1) - 1\right] + 2}. \quad (11)$$

Equation (7) is integrated over the volume of irradiated material for both the incident and primary scattered beams to obtain the total secondary scattering intensity at O_3. The differential intensity is described by equation (7), but it should be noted that the bounds on the integral are geometry dependent.

By convention (Warren & Mozzi, 1966; Dwiggins, 1972, 1975), the ratio of secondary to primary scattering is reported in the form of equation (12), where Q_M is the geometry-dependent integral, which can be solved given μt, 2θ, ϕ and $J(2\theta)/\sum \chi_i {Z_i}^2$, and summations are performed over elemental species i,

$$\frac{I_2}{I_1}(2\theta, \phi) = \frac{\left(\sum \chi_i {Z_i}^2\right)^2 Q_M}{J(2\theta)\sum \chi_i M_i (\mu/\rho)_i}. \quad (12)$$

3. Absorption for off-central-axis beam

For a beam of cross-sectional area dA_0 that is incident off-center by a radial distance x and at the angle ξ_0 onto a sample of radius r_s, the scattering volume is a triple integral over the area of the beam (beam radius and angle) and the sample thickness, as shown in Fig. 3.

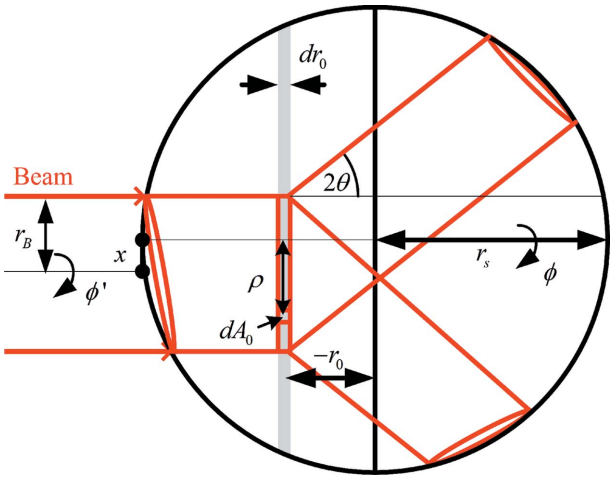

Figure 3
Geometry of scattering from a spherical sample.

The effective scattering volume for a spherical sample in this case is described by equation (13), where $R(r_0, 2\theta, \phi, \rho, \xi)$ is the position-dependent travel length of the diffracted beam and $\mathrm{d}A_0(\phi', r')$ is the differential area of the principal beam,

$$V'_{\rm Sphere}(2\theta,\phi) = \int\int \mathrm{d}A_0(\phi', r') \int_{-(r_s^2-\rho^2)^{1/2}}^{(r_s^2-\rho^2)^{1/2}} \mathrm{d}r_0 \times \exp[-\mu r_0 - \mu(r_s^2-\rho^2)^{1/2} - \mu R(r_0, 2\theta, \phi, \rho, \xi)]. \quad (13)$$

The function $R(r_0, 2\theta, \phi, \rho, \xi)$ can be obtained from the intersection between a cone centered at the origin pointing in the $+z$ direction and a sphere shifted by a distance r_0 along the z axis and centered in the x–y plane at an angle ξ from the x axis and radial distance ρ, as shown in Fig. 4. The path length from the position r_0, ρ, ξ to the surface of a sphere along the solid angle 2θ, ϕ is described by

$$\begin{aligned} R(r_0, 2\theta, \phi, \rho, \xi) = {} & \rho\sin(2\theta)\cos(\phi-\xi) - r_0\cos(2\theta) \\ & + [r_0^2\cos^2(2\theta) - r_0^2 - \rho^2 + r_s^2 \\ & - 2r_0\rho\cos(2\theta)\sin(2\theta)\cos(\phi-\xi) \\ & + \rho^2\sin^2(2\theta)\cos^2(\phi-\xi)]^{1/2}. \end{aligned} \quad (14)$$

Given any arbitrary beam shape and incidence, the effective scattering volume can be obtained by numerically integrating equations (13) and (14).

For a circular beam that is centered off the central axis, equation (13) becomes equation (15) with the x axis aligned such that $\xi_0 = 0$,

$$V'_{\rm Sphere}(2\theta,\phi) = \int_0^{r_B} r'\,\mathrm{d}r' \int_0^{2\pi} \mathrm{d}\phi' \int_{-(r_s^2-\rho^2)^{1/2}}^{(r_s^2-\rho^2)^{1/2}} \mathrm{d}r_0 \times \exp[-\mu r_0 - \mu(r_s^2-\rho^2)^{1/2} - \mu R(r_0, 2\theta, \phi, \rho, \xi)], \quad (15)$$

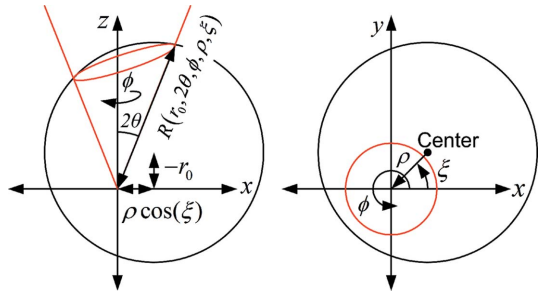

Figure 4
Perpendicular views of the geometry of a diffraction cone intersecting a spherical sample.

where $\rho = \{[r'\cos(\phi') + x]^2 + r'^2\sin(\phi')^2\}^{1/2}$, $\xi = \tan^{-1}\{r'\sin(\phi')/[r'\cos(\phi') + x]\} - \pi$, and r' and ϕ' are beam coordinates.

It is useful to scale by units of the sample radius; here any scaled quantity is denoted by the subscript 's' (*e.g.* $\alpha/r_s = \alpha_s$). This reduces the number of parameters from four (μ, r_B, r_s, x) to three (μr_s, r_{Bs}, x_s) as shown in equations (16) and (17),

$$V'_{\rm Sphere} = r_s r_B^2 \int_0^1 r'_s\,\mathrm{d}r'_s \int_0^{2\pi} \mathrm{d}\phi' \int_{-(1-\rho_s^2)^{1/2}}^{(1-\rho_s^2)^{1/2}} \mathrm{d}r_{0s} \times \exp[-\mu r_s r_{0s} - \mu r_s(1-\rho_s^2)^{1/2} - \mu r_s R_s(r_{0s}, 2\theta, \phi, \rho_s, \xi)], \quad (16)$$

$$\begin{aligned} R_s(r_{0s}, 2\theta, \phi, \rho_s, \xi) = {} & \rho_s\sin(2\theta)\cos(\phi-\xi) - r_{0s}\cos(2\theta) \\ & + [r_{0s}^2\cos^2(2\theta) - r_{0s}^2 - \rho_s^2 + 1 \\ & - 2r_{0s}\rho_s\cos(2\theta)\sin(2\theta)\cos(\phi-\xi) \\ & + \rho_s^2\sin^2(2\theta)\cos^2(\phi-\xi)]^{1/2}, \end{aligned} \quad (17)$$

where $\rho_s = \{[r'_s r_{Bs}\cos(\phi') + x_s]^2 + r'^2_s(r_{Bs})^2\sin(\phi')^2\}^{1/2}$ and $\xi = \tan^{-1}\{r'_s r_{Bs}\sin(\phi')/[r'_s r_{Bs}\cos(\phi') + x_s]\} - \pi$.

The integral in equation (16) has no closed-form solution. In the small-beam limit, $r_{Bs} \rightarrow 0$, two of the integrals become trivial as shown by equation (18). The spherical correction can then be easily computed numerically,

$$V'_{\rm Sphere} = \pi r_s r_B^2 \exp\big[-\mu r_s(1-x_s^2)^{1/2}\big] \int_{-(1-x_s^2)^{1/2}}^{(1-x_s^2)^{1/2}} \mathrm{d}r_{0s} \times \exp\big[-\mu r_s r_{0s} - \mu r_s R_s(r_{0s}, 2\theta, \phi, x_s, \xi)\big]. \quad (18)$$

If a numerical solution is too computationally expensive, such as when using fitting algorithms, an analytic expansion in the small-angle limit $2\theta \rightarrow 0$ may be used.

The asymptotic expansion of the absorption correction for a zero-width beam is given by equation (19), where the first six coefficients are specified in Table 2,

Table 2
Coefficients for small-angle expansion of the off-axis spherical absorption.

i	A_i
0	1
1	$\cos(\phi)\mu r_s x_s$
2	$\frac{\mu r_s}{6(x_s^2-1)}[2\mu r_s\cos(\phi)^2 x_s^4 - x_s^2(1-x_s^2)^{1/2} - 2\mu r_s\cos(\phi)^2 x_s^2 + (1-x_s^2)^{1/2} - 2x_s^2\cos(\phi)^2(1-x_s^2)^{1/2}]$
3	$\frac{x_s\cos(\phi)\mu r_s}{6(x_s^2-1)}[2\mu r_s\cos(\phi)^2 x_s^2(1-x_s^2)^{1/2} + x_s^2 - 1]$
4	$\frac{\mu r_s}{360(x_s^2-1)}[8(\mu r_s)^3 x_s^6\cos(\phi)^4 + 40\mu r_s x_s^4\cos(\phi)^4 - 14\mu r_s x_s^4 + 32(\mu r_s)^2 x_s^4\cos(\phi)^4(1-x_s^2)^{1/2} - 8(\mu r_s)^3 x_s^4\cos(\phi)^4 - 32(\mu r_s)^2 x_s^4\cos(\phi)^2(1-x_s^2)^{1/2} + 44\mu r_s x_s^4\cos(\phi)^2 - 11(1-x_s^2)^{1/2}x_s^2 - 4x^2\cos(\phi)^2(1-x_s^2)^{1/2} - 44\mu r_s x_s^2\cos(\phi)^2 + 32(\mu r_s)^2 x_s^2\cos(\phi)^2(1-x_s^2)^{1/2} + 11(1-x_s^2)^{1/2} - 14\mu r_s + 28\mu r_s x_s^2]$
5	$\frac{\mu r_s x_s\cos(\phi)}{360(x_s^2-1)}[8(\mu r_s)^3 x_s^4\cos(\phi)^4(1-x_s^2)^{1/2} + 16(\mu r_s)^2 x_s^4 - 40(\mu r_s)^2 x_s^4\cos(\phi)^4 + 8(\mu r_s)^3 x_s^4\cos(\phi)^2(1-x_s^2)^{1/2} + 24(\mu r_s)^2 x_s^4\cos(\phi)^2 + 3x_s^2 - 6\mu r_s x_s^2(1-x_s^2)^{1/2} - 3 + 16(\mu r_s)^2 - 8(\mu r_s)^3 x_s^2\cos(\phi)^2(1-x_s^2)^{1/2} + 6\mu r_s(1-x_s^2)^{1/2} - 32(\mu r_s)^2 x_s^2 + 36\mu r_s x_s^2\cos(\phi)^2(1-x_s^2)^{1/2} - 24(\mu r_s)^2 x_s^2\cos(\phi)^2]$

$$\frac{V}{V'} \sim \exp\left[2\mu r_s(1-x_s^2)^{1/2}\right]/(1-x_s^2)^{1/2} \times \sum_{i=0}^{\infty} A_i(\mu r_s, x_s, \phi)(2\theta)^i, \quad 2\theta \to 0, \quad r_{Bs} = 0. \tag{19}$$

This correction must be applied to two-dimensional data since it can manifest itself as a large gradient in intensity across the detector. Although the higher-order terms in the $r_{Bs} \to 0$ expansion are valid corrections for $x_s + r_{Bs} < 1$, as parts of the beam miss the sample (*i.e.* for $x_s + r_{Bs} > 1$), these terms diverge from the numerical solution while the lowest-order term remains accurate.

4. Secondary scattering for off-central-axis beam

In this section, a numerical solution for the secondary scattering geometry, as illustrated in Fig. 5, is presented.

The bounds of integration for the secondary scattering integrals are defined by the two illuminated volumes, *i.e.* of the principal beam and primary diffraction cones (refer to Fig. 3). For the principal beam this volume is given by

$$\int_0^{r_B} r'\,dr' \int_0^{2\pi} d\phi' \int_{-(r_s^2-\rho^2)^{1/2}}^{(r_s^2-\rho^2)^{1/2}} dr_0. \tag{20}$$

The volume of the primary diffraction cone originating from the point (r_0, ρ, ξ) is obtained by an integral over $2\theta_1$, ϕ_1 and the path length from the diffracting volume to the edge of the sphere,

$$\int_0^{\pi} \sin(2\theta_1)\,d2\theta_1 \int_0^{2\pi} d\phi_1 \int_0^{R(r_0,2\theta_1,\phi_1,\rho,\xi)} r_1^2\,dr_1. \tag{21}$$

The two-volume integral, for secondary scattering in an arbitrary spherical geometry, is described by

$$I_2(2\theta,\phi) = \left(I_0 n^2\sigma_e^2/r^2\right) \int_0^{r_B} r'\,dr' \int_0^{2\pi} d\phi' \int_{-(r_s^2-\rho^2)^{1/2}}^{(r_s^2-\rho^2)^{1/2}} dr_0 \times \int_0^{\pi} \sin(2\theta_1)\,d2\theta_1 \int_0^{2\pi} d\phi_1 \int_0^{R(r_0,2\theta_1,\phi_1,\rho,\xi)} dr_1 \times \exp[-\mu r_0 - \mu r_1 - \mu(r_s^2-\rho^2)^{1/2} - \mu R(z_1, 2\theta, \phi, \rho_1, \xi_1)] \times P(\kappa_0, 2\theta_1, \phi_1)J(2\theta_1)P(\kappa_1, 2\theta_2, \phi_2)J(2\theta_2). \tag{22}$$

The path length from the secondary scattering volume to the surface of the sphere is $R(z_1, 2\theta, \phi, \rho_1, \xi_1)$, where (z_1, ρ_1, ξ_1) is the point of secondary scattering in cylindrical coordinates. The values of z_1, ρ_1 and ξ_1 are defined by $z_1 = r_0 + r_1\cos(2\theta_1)$,

$$\xi_1 = \tan^{-1}\left\{\frac{r'\sin(\phi') + r_1\sin(2\theta_1)\sin(\phi_1)}{[r'\cos(\phi') + x] + r_1\sin(2\theta_1)\cos(\phi_1)}\right\} - \pi$$

and

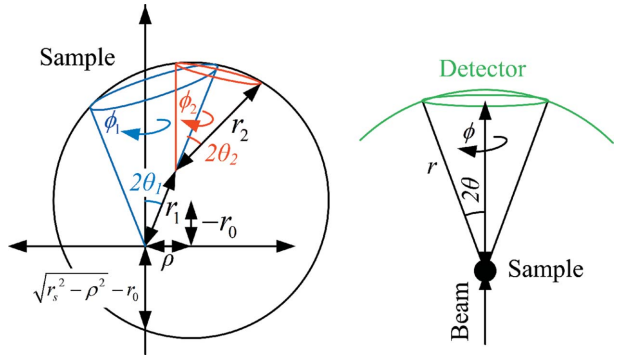

Figure 5
The geometry of a secondary diffraction cone intersecting a spherical sample.

$$\rho_1 = \{[r'\cos(\phi') + x + r_1\sin(2\theta_1)\cos(\phi_1)]^2 + [r'^2\sin(\phi') + r_1\sin(2\theta_1)\sin(\phi_1)]^2\}^{1/2}.$$

As with the spherical absorption correction, the number of parameters can be reduced by scaling to r_s, yielding

$$\begin{aligned} I_2(2\theta,\phi) = {} & \left(I_0 r_s^4 n^2 \sigma_e^2 / r^2\right) \int_0^{r_{Bs}} r_s' \, dr_s' \int_0^{2\pi} d\phi' \int_{-(1-\rho_s^2)^{1/2}}^{(1-\rho_s^2)^{1/2}} dr_{0s} \\ & \times \int_0^{\pi} \sin(2\theta_1)\, d2\theta_1 \int_0^{2\pi} d\phi_1 \int_0^{R_s(r_{0s},2\theta_1,\phi_1,\rho_s,\xi)} dr_{1s} \\ & \times \exp[-\mu r_s r_{0s} - \mu r_s r_{1s} - \mu r_s (1-\rho_s^2)^{1/2} \\ & - \mu r_s R_s(z_{1s}, 2\theta, \phi, \rho_{1s}, \xi_1)] \\ & \times P(\kappa_0, 2\theta_1, \phi_1) J(2\theta_1) P(\kappa_1, 2\theta_2, \phi_2) J(2\theta_2). \end{aligned} \tag{23}$$

The evaluation of equation (23) is made more difficult by the finite size of the beam. In the small-beam limit, however, two of the six integrals become trivial and $\rho \rightarrow x$ such that equation (22) reduces to

$$\begin{aligned} I_2(2\theta,\phi) = {} & \left(I_0 \pi r_B^2 r_s^2 n^2 \sigma_e^2 / r^2\right) \int_{-(1-x_s^2)^{1/2}}^{(1-x_s^2)^{1/2}} dr_{0s} \\ & \times \int_0^{\pi} \sin(2\theta_1)\, d2\theta_1 \int_0^{2\pi} d\phi_1 \int_0^{R_s(r_{0s},2\theta_1,\phi_1,x_s,\xi)} dr_{1s} \\ & \times \exp[-\mu r_s r_{0s} - \mu r_s r_{1s} - \mu r_s (1-x_s^2)^{1/2} \\ & - \mu r_s R_s(z_{1s}, 2\theta, \phi, \rho_{1s}, \xi_1)] \\ & \times P(\kappa_0, 2\theta_1, \phi_1) J(2\theta_1) P(\kappa_1, 2\theta_2, \phi_2) J(2\theta_2). \end{aligned} \tag{24}$$

Since the corrected intensity is described by equation (4), the ratio of secondary scattering intensity to primary scattering intensity is given by

$$\begin{aligned} & I_2(2\theta,\phi)/I_1(2\theta,\phi) = \\ & \left\{r_s n \sigma_e V / \left[2P(\kappa_0, 2\theta, \phi) J(2\theta) V'\right]\right\} \int_{-(1-x_s^2)^{1/2}}^{(1-x_s^2)^{1/2}} dr_{0s} \\ & \times \int_0^{\pi} \sin(2\theta_1)\, d2\theta_1 \int_0^{2\pi} d\phi_1 \int_0^{R_s(r_{0s},2\theta_1,\phi_1,x,\xi)} dr_{1s} \\ & \times \exp[-\mu r_s r_{0s} - \mu r_s r_{1s} - \mu r_s (1-x_s^2)^{1/2} \\ & - \mu r_s R_s(z_{1s}, 2\theta, \phi, \rho_{1s}, \xi_1)] \\ & \times P(\kappa_0, 2\theta_1, \phi_1) J(2\theta_1) P(\kappa_1, 2\theta_2, \phi_2) J(2\theta_2). \end{aligned} \tag{25}$$

To convert this to the form of equation (12), the substitution $r_s n \sigma_e = \sigma_e N_A \mu r_s / \sum \chi_i M_i (\mu/\rho)_i$ is made so that Q_M for offset spherical geometry is given by

$$\begin{aligned} Q_M = {} & \left\{N_A \sigma_e \mu r_s V / \left[2P(\kappa_0, 2\theta, \phi) V'\right]\right\} \int_{-(1-x_s^2)^{1/2}}^{(1-x_s^2)^{1/2}} dr_{0s} \\ & \times \int_0^{\pi} \sin(2\theta_1)\, d2\theta_1 \int_0^{2\pi} d\phi_1 \int_0^{R_s(r_{0s},2\theta_1,\phi_1,x,\xi)} dr_{1s} \\ & \times \exp[-\mu r_s r_{0s} - \mu r_s r_{1s} - \mu r_s (1-x_s^2)^{1/2} \\ & - \mu r_s R_s(z_{1s}, 2\theta, \phi, \rho_{1s}, \xi_1)] \\ & \times P(\kappa_0, 2\theta_1, \phi_1) J(2\theta_1) P(\kappa_1, 2\theta_2, \phi_2) J(2\theta_2) / \left(\sum \chi_i Z_i^2\right)^2. \end{aligned} \tag{26}$$

The large number of parameters makes the tabulation of Q_M difficult. Instead, it can be obtained from a numerical integration, given values of κ_0, x_s, μr_s, 2θ, ϕ and $J(2\theta)/\left(\sum \chi_i Z_i^2\right)$.

Since $J(2\theta)$ is unknown, the computation of Q_M, which is independent of the experimental data, may be obtained if $J(2\theta)$ is approximated by $\sum \chi_i [f_i^2 + i(M)_i]$ (Warren & Mozzi, 1966; Dwiggins & Park, 1971; Dwiggins, 1972). Unlike for standard transmission and reflection geometries, the analytic approximation for $J(2\theta)/\left(\sum \chi_i Z_i^2\right) = q + \{(1-q)/[1 + b\sin^2(\theta)]\}$ (Warren & Mozzi, 1966; Dwiggins & Park, 1971; Dwiggins, 1972) provides little benefit here. The approximation for $J(2\theta)$ as the average atomic scattering intensity diverges strongly from the true values of $J(2\theta)$ at small angles and, therefore, may not be appropriate for small-angle data with large μr_s. Following Malet *et al.* (1973), the experimental $I(2\theta)$, after removing polarization and absorption effects and scaling to electron units, is used as an approximate form of $J(2\theta)$ in the secondary scattering integral. Practically, the experimental $I(2\theta)$ is limited to some $2\theta_{max}$ after which the $\sum \chi_i [f_i^2 + i(M)_i]$ approximation is appropriate. The suggested approximation for $J(2\theta)$ is shown in equation (27) where the normalization constant N is chosen to match the two approximate forms of $J(2\theta)$ at $2\theta_{max}$,

$$J(2\theta) \simeq \begin{cases} \dfrac{1}{N}\dfrac{1}{2\pi}\displaystyle\int_0^{2\pi} d\phi \dfrac{I(\phi, 2\theta) V}{P(\kappa_0, 2\theta, \phi) V'} & \text{for } 2\theta \leq 2\theta_{max}, \\ \sum \chi_i \left[f_i^2 + i(M)_i\right] & \text{for } 2\theta \geq 2\theta_{max}. \end{cases} \tag{27}$$

In principle, the calculation of I_2/I_1 can be iterated with successively better approximations for $J(2\theta)$; however, this is too computationally intensive to be practical.

5. Results and discussion

Three special cases of the integral forms of absorption and secondary scattering derived in the previous section for an X-ray beam incident on a spherical amorphous sample are of particular interest. The first is the case of a non-polarized beam incident on the center of the sample ($x_s = 0$, $\kappa_0 = 0$). For the second case, where the incident beam is off to one side of the central axis, the asymmetry in the measured intensity is greatest for strongly absorbing samples. To illustrate this, we chose $x_s > 0$ and $2\mu r_s = 10$. For the third, the average corrections about the azimuthal angle are evaluated, indicating that there remains a strong dependence of the correc-

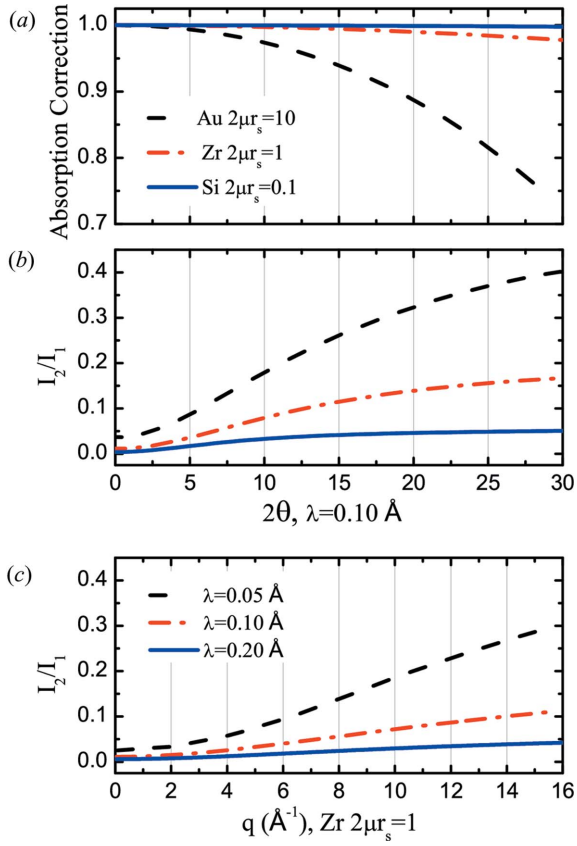

Figure 6
Dependence of the absorption correction (*a*) and secondary scattering intensity on attenuation (*b*) and energy (*c*) in centered spherical geometry.

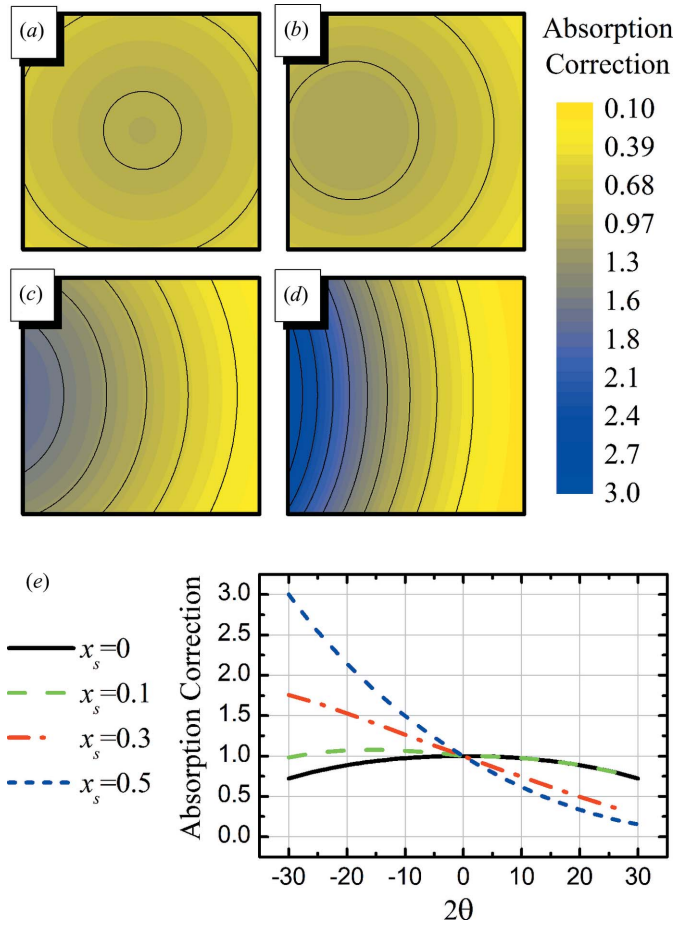

Figure 7
Simulated two-dimensional detector image asymmetry in the absorption correction normalized to the beam center for $2\mu r_s = 10$ caused by off-axis beam incidence at (*a*) $x_s = 0$, (*b*) $x_s = 0.1$, (*c*) $x_s = 0.3$ and (*d*) $x_s = 0.5$, and (*e*) along the x axis ($\phi = 0$).

tion on the degree of off-axis transmission after angular averaging. Unless otherwise noted, synchrotron wavelengths ($\simeq 0.1$ Å) were used for calculations of I_2/I_1.

The first case is unique; both the absorption and secondary scattering corrections are symmetric in ϕ so that they can be applied directly to the one-dimensional $I(q)$ data, obtained by a circular average of the detector intensity as a function of q. The calculated spherical absorption corrections normalized to $\exp(-2\mu r_s)$ for $2\mu r_s = 0.1$, 1 and 10 are shown in Fig. 6(*a*). The secondary scattering corrections for the same μr_s are also shown (Fig. 6*b*). For these calculations, the $J(2\theta)$'s were taken to have the form of the atomic scattering factor for Si, Zr and Au. These elements have the appropriate densities and linear absorption coefficients at synchrotron wavelengths to attain these values of μr_s for samples sizes that are appropriate for the beamline ESL (Mauro & Kelton, 2011). The absorption corrections shown in Fig. 6 were computed numerically, although a fifth-order asymptotic expansion, equation (19), agrees to within 2% at $2\theta = 30^\circ$ for $2\mu r_s = 10$, and is indistinguishable from the numerical solution for $2\mu r_s = 1$. The secondary scattering also depends on wavelength through $J(2\theta)$, as shown in Fig. 6(*c*): higher energy (*i.e.* lower wavelength) results in a more rapid increase of I_2/I_1 with momentum transfer and diffraction angle (not shown).

Off-central-axis alignment, the second case, results in a dramatically asymmetric detector intensity pattern, requiring a two-dimensional correction. Figs. 7(*a*)–7(*d*) show the absorption correction for the intensity measured with an area detector for $2\mu r_s = 10$ for $x_s = 0$, 0.1, 0.3 and 0.5, respectively. The absorption correction as a function of scattering angle, 2θ, for the $\phi = 0$ axis, using the same values of $2\mu r_s$, is shown in Fig. 7(*e*). The secondary scattering intensities, assuming values for Au, $\kappa_0 = 0$, $2\mu r_s = 10$, and $x_s = 0$, 0.1, 0.3 and 0.5, are shown in Figs. 8(*a*)–8(*d*), respectively. The ratios of secondary to primary scattering intensities as a function of 2θ, for $\phi = 0$, are shown in Fig. 8(*e*). The asymmetry observed in the measured intensity due to the incidence of the X-ray beam off-incidence with the axis through the center of the sample is dominated by absorption corrections. However, a corresponding asymmetry in the secondary scattering correction is also found.

Since the integral average around the azimuthal angle is often taken for symmetric area detectors, the effect of misalignment on the angular averaged corrections is considered. As shown in Fig. 9 for Au, $2\mu r_s = 10$ and $x_s = 0$, 0.1, 0.3, 0.5 and 0.8, the curvature of the averaged absorption correction changes dramatically with increasing x_s, from negative curvature at near-central-axis alignment to positive curvature as the degree of misalignment increases. Also shown in Fig. 9,

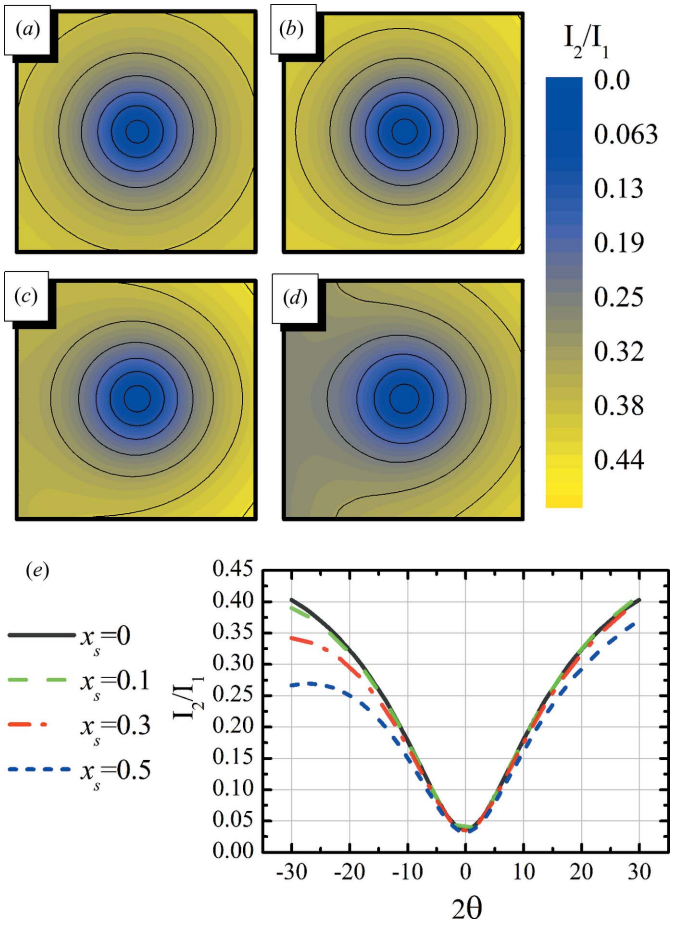

Figure 8
Simulated two-dimensional detector image asymmetry in the secondary scattering intensity of Au, $2\mu r_s = 10$, at $\lambda = 0.1$ caused by off-axis beam incidence at (*a*) $x_s = 0$, (*b*) $x_s = 0.1$, (*c*) $x_s = 0.3$ and (*d*) $x_s = 0.5$, and (*e*) comparison of line profiles of intensity across the x axis.

the angular averaged secondary scattering intensity systematically decreases with increasing x_s. From perturbations of $2\mu r_s$ and λ about the Zr, $2\mu r_s = 1$, $\lambda = 0.1$ case, the parameter space in which the angular average correction remains within 1% of the centrally aligned beam case ($x_s = 0$) at $2\theta = 30^\circ$ is bound by $x_s < [0.45 - 0.2\ln(2\mu r_s) + 3.2\,\text{Å}^{-1}(\lambda - 0.1\,\text{Å})]$. Within this region of parameter space the centrally aligned beam may be used as an approximation of the offset spherical absorption correction.

In situations where the sample cannot be accurately aligned using a transmission measurement, the degree and angle of off-central-axis alignment (*i.e.* x_s and ξ_0) may be unknown. Since liquids are isotropic, $J(2\theta)$ should be axially symmetric, so these parameters can be solved using the observed detector asymmetry. For an area detector that is perpendicular, or tilt corrected, to the transmitted X-ray beam and has been background and gain corrected, any asymmetry present in the detected scattering intensity from the amorphous samples can be attributed to polarization effects and an X-ray beam that is displaced from the central axis of the sample. The polarization effects are described by equation (2). After making the polarization correction, the azimuthal angle of maximum

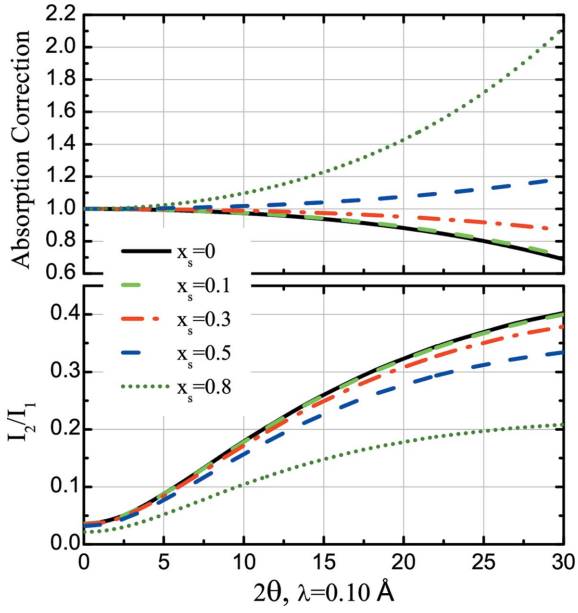

Figure 9
Azimuthal averaged absorption correction (upper) and secondary scattering intensity (lower) with off-central-axis alignment.

intensity at constant 2θ identifies the angle of the offset in Fig. 3 ($\xi_0 + \pi$). A non-linear fitting approach may then be used to determine the value of x_s that removes the asymmetry from the detector image.

6. Concluding remarks

Corrections to improve the analysis of scattering data studies from liquids are critically important. The artifacts arising from an improper alignment of the sample, such as asymmetric absorption and secondary scattering intensity, can produce poor data that cannot be analyzed quantitatively. This paper presents the development of corrections for absorption and secondary scattering intensity when a partially polarized X-ray beam of size smaller than the size of a liquid sample processed in a containerless environment is incident upon the sample, but displaced from the central axis. While the corrections obtained are expressed in integral form, current computing resources allow rapid evaluations for any given set of parameters.

This research was partially supported by the National Science Foundation under grant Nos. DMR-12-06707 and DMR-08-56199, and NASA under grant Nos. NNX07AK27G and NNX10AU19G.

References

Aoki, H., Paradis, P.-F., Ishikawa, T., Aoyama, T., Masaki, T., Yoda, S., Ishii, Y. & Itami, T. (2003). *Rev. Sci. Instrum.* **74**, 1147–1149.
Blech, I. A. & Averbach, B. L. (1965). *Phys. Rev.* **137**, A1113.
Coppens, P., Cox, D., Vlieg, E. & Robinson, I. (1992). *Synchrotron Radiation Crystallography*. San Diego: Academic Press.
Dwiggins, C. W. Jr (1972). *Acta Cryst.* A**28**, 158–163.

Dwiggins, C. W. Jr (1975). *Acta Cryst.* A**31**, 395–396.
Dwiggins, C. W. Jr & Park, D. A. (1971). *Acta Cryst.* A**27**, 264–272.
Egry, I. & Holland-Moritz, D. (2011). *Eur. Phys. J. Special Topics*, **196**, 131–150.
Gangopadhyay, A. K., Lee, G. W., Kelton, K. F., Rogers, J. R., Goldman, A. I., Robinson, D. S., Rathz, T. J. & Hyers, R. W. (2005). *Rev. Sci. Instrum.* **76**, 073901.
Higuchi, K., Kimura, K., Mizuno, A., Watanabe, M., Katayama, Y. & Kuribayashi, K. (2007). *J. Non-Crystalline Solids*, **353**, 2997–2999.
Kahn, R., Fourme, R., Gadet, A., Janin, J., Dumas, C. & André, D. (1982). *J. Appl. Cryst.* **15**, 330–337.
Krishnan, S., Felten, J. J., Rix, J. E., Weber, J. K. R., Nordine, P. C., Beno, M. A., Ansell, S. & Price, D. L. (1997). *Rev. Sci. Instrum.* **68**, 3512–3518.
Malet, G., Cabos, C., Escande, A. & Delord, P. (1973). *J. Appl. Cryst.* **6**, 139–144.
Masaki, T., Ishikawa, T., Paradis, P.-F., Yoda, S., Okada, J. T., Watanabe, Y., Nanao, S., Ishikura, A., Higuchi, K., Mizuno, A., Watanabe, M. & Kohara, S. (2007). *Rev. Sci. Instrum.* **78**, 026102.
Mauro, N. A. & Kelton, K. F. (2011). *Rev. Sci. Instrum.* **82**, 035114.
Paalman, H. H. & Pings, C. J. (1962). *J. Appl. Phys.* **33**, 2635–2639.
Warren, B. E. & Mozzi, R. L. (1966). *Acta Cryst.* **21**, 459–461.
Zeidler, A. (2012). *J. Appl. Cryst.* **45**, 122–123.